Journal of Molecular Structure 1345 (2025) 143018

Contents lists available at ScienceDirect

Journal of Molecular Structure

journal homepage: www.elsevier.com/locate/molstr

Structural and photoelectric properties of ionic liquid crystals tuned by CdS and carbon quantum dots

D. Zhulai [a,c,*], N. Boichuk [a], D. Pustovyi [a], G. Beltramo [b], O. Kovalchuk [c,e], Y. Garbovskiy [f], G. Klimusheva [c], G. Yaremchuk [d], T. Mirnaya [d], S. Vitusevich [a]

[a] Forschungszentrum Jülich GmbH, Institute of Biological Information Processing – Bioelectronics (IBI-3) 52428 Jülich, Germany
[b] Forschungszentrum Jülich GmbH, Institute of Biological Information Processing – Mechanobiology (IBI-2) 52428 Jülich, Germany
[c] Institute of Physics of NAS of Ukraine 03028 Kyiv, Ukraine
[d] V.I. Vernadsky Institute of General and Inorganic Chemistry of NAS of Ukraine 03142 Kyiv, Ukraine
[e] Kyiv National University of Technologies and Design 01011 Kyiv, Ukraine
[f] Department of Physics and Engineering Physics, Central Connecticut State University, New Britain, CT, USA

ARTICLE INFO

Keywords:
Nanoparticles
Ionic liquid crystals
Nanocomposite materials
Raman spectroscopy
Optical spectroscopy
Tauc plot
Brus equation
Photovoltaics
Dember effect

ABSTRACT

Glass-like materials with quantum dots (QDs) represent a new class of electro-optical structures with unique properties. The photoelectric and physical characteristics of these structures can be precisely adjusted using QDs of a specific size and composition, making them attractive for a numerous potential applications. These nanocomposite materials are promising for various research fields including optoelectronics, photonics, sensing, electrochemistry, catalysis and biomedicine. In this article we studied cadmium octanoate $Cd^{+2}(C_7H_{15}COO^-)_2$ (abbreviation CdC_8) ionic liquid crystal (ILC) with several types of QDs, cadmium sulfide (CdS) and carbon (C) QDs, as well as both these QDs. A distinctive property of the CdC_8 matrix acting as a nanoreactor is the possibility of controlling the size and uniformity of QDs during the synthesis. The Raman spectra of the CdC_8 matrix were studied to characterize molecular vibrations and identify features of chemical bonds and functional groups. Nanocomposite materials including two types of QDs in the CdC_8 matrix were investigated. The shape and size of the QDs were measured using transmission electron microscopy (TEM). The mode diameter of the CdS QDs are estimated to be 2.5 nm, while that of the C QDs is 8.2 nm. The obtained data were used to analyze the correlation between the structural characteristics of QDs and their optical properties. The spectral characteristics of CdS QDs, C QDs, and their combinations were studied. Temperature effects reflecting spectral shift of the CdS QDs maximum from 322 nm to 333 nm and a decrease of the band gap from 3.63 eV to 3.56 eV, calculated using Tauc plot were studied. The diameter of CdS QDs, calculated from the optical spectra using the Brus equation, was found to be about 2.7 nm, which is in good agreement with the TEM data.

The photovoltaic properties of these materials have been studied using UV light sources in temperature range from 20 °C to 130 °C. Adding of CdS QDs and C QDs to the CdC_8 matrix improves the photovoltaic properties of the material due to the Dember effect. The highest photocurrent was observed in the CdC_8 matrix with the combination of C QDs and CdS QDs, indicating a synergistic effect between the two types of QDs resulting in an optimized photovoltaic response. The results demonstrate that synthesized nanomaterials have great potential for the design of photoelectric elements and optical sensors.

1. Introduction

The design of nanomaterials represents the fundamental key to the improvement of performance, sensitivity, and durability of newly developed optoelectronic devices. These devices perform various functions, including the generation [1,2], processing, transmission, and detection of light [3–6]. They can be used as light sources [7] as well as light receivers [8]. Their efficiency directly depends on the optical and electronic properties of the constituent materials. Therefore, one of the main areas of current research in optoelectronics is the development of new nanomaterials and the improvement of existing ones.

Classical silicon (Si) and gallium arsenide (GaAs) semiconductors

* Corresponding author.
E-mail address: d.zhulai@fz-juelich.de (D. Zhulai).

https://doi.org/10.1016/j.molstruc.2025.143018
Received 29 January 2025; Received in revised form 16 May 2025; Accepted 16 June 2025
Available online 22 June 2025

form the basis for the development of optoelectronic technologies. Device structures fabricated on the basis of these materials are highly sensitive to visible and infrared light [9,10] and are stable. Si is widely used in photodetectors, especially in integrated circuits, due to its compatibility with existing technologies. However, its sensitivity is limited in the ultraviolet and infrared ranges. GaAs is preferred for high-frequency devices [11] and solar cells [12]. It is more sensitive to infrared light and provides a faster response time [13]. However, the spectral sensitivity and flexibility of these materials are limited.

Over recent years, nanostructured materials including QDs, nanowires, and 2D materials were attracting attention due to their unique optical and electronic properties, which significantly enhance the capabilities of traditional semiconductors. QDs are ideal for optimizing photosensitivity in a variety of devices due to the quantum size effect, which allows their energy structure to be adjusted by changing their size [14]. New technologies for the development of nanocomposite materials [15] are particularly important today, as they can significantly improve the characteristics and performance of optoelectronic devices.

Therefore, it is a great challenge for researchers to synthesize QDs with a controllable size and stable properties [16–18]. The shape, size, and uniform distribution of QDs in a material must be precisely controlled to ensure the efficient operation of optoelectronic devices. These characteristics directly affect the optical and electronic properties of device structures and, in turn, overall device performance.

Integrating CdS and C QDs into hybrid materials, such as organometallic-based matrices, can significantly enhance their electro-optical performance and improve the overall performance of optoelectronic devices. This opens up the possibility of creating attractive multifunctional materials that can simultaneously perform several tasks and extend the functionality of current technologies. However, systematic studies were focused mainly on nematic liquid crystals, where the impact of CdS and C QDs on their physicochemical properties are investigated [19,20]. At the same time, ILCs stand out as materials that combine ionic conductivity with the self-organizing structure of liquid crystals [21,22]. Specifically, the smectic A phase of ILC is characterized by a layered molecular organization, which can facilitate the ordered distribution of nanoparticles [23] and the creation of stable composites with tunable optical and electrochemical properties. Despite the growing interest in ILCs as host media, studies of their compositions with different types of QDs remain limited. Moreover, studies on nanocomposites including ILC with two different QDs, such as CdS QDs and C QDs, are still lacking. The approach of introducing two QDs, may provide synergistic effects by combining the unique optical and electronic properties of each type of QDs, potentially leading to the development of multifunctional materials with enhanced properties.

In this work, the fundamental spectral and electro-optical properties of novel nanocomposites with CdS QDs and C QDs chemically synthesized in the smectic A phase of ILC cadmium octanoate CdC_8 were investigated. In addition, previously missed in the literature Raman spectra of the CdC_8 matrix were studied to characterize molecular vibrations and identify features of chemical bonds and functional groups to analyze the obtained nanocomposite materials in more detail. The results of these studies provide a new perspective on the role of the QDs in the electro-optical performance of these multi-functional materials. We also considered how QDs affect photovoltaic properties of nanocomposite materials. The obtained results open up new perspectives for developing high-performance optoelectronic devices, photodetectors, sensors, and other technologies based on such advanced nanocomposite materials.

2. Materials and methods

The CdC_8 matrix can be used as a nanoreactor [24] for the synthesis of semiconducting QDs as well as metallic and hybrid (core/shell and bimetallic) nanoparticles. Already synthesized nanoparticles have shown promising nonlinear optical [25–28] and interesting photo-electrical properties [29–31].

Cadmium octanoate CdC_8 (Fig. 1A) was used as a nanoreactor (Fig. 1B) to synthesize CdS QDs (Fig. 1C). CdC_8 undergoes a phase transition from a crystalline phase at room temperature to a smectic A phase at temperature above 98 °C and to an isotropic phase at temperature > 180 °C. Important features of this synthesis are that CdS QDs do not stick together throughout and no aggregation occurs in the CdC_8 matrix. The reason is that the CdC_8 matrix acts as a reducing agent for the CdS QDs. The concentration of CdS QDs in the CdC_8 matrix is further given in the text in molar percent (mol. %) as these QDs were synthesized directly within the CdC_8 matrix, allowing for a precise calculation of the molar ratio. C QDs were pre-synthesized separately from the CdC_8 matrix [32] because their synthesis temperature is incompatible with the synthesis conditions inside the CdC_8 matrix. Therefore, the weight percentage calculation (wt %) was used to express an amount of C QDs added to CdC_8 matrix. The synthesized C QDs were combined with the CdC_8 matrix to ensure their integration into the material composition (Fig. 1D).

In order to obtain a nanocomposite with two types of QDs, the synthesized CdS QDs with a CdC_8 matrix were combined with C QDs to form a hybrid nanocomposite. Using this approach, we have efficiently integrated both types of QDs into a single structure to ensure that they would interact at the nanoscale. The concentration of CdS QDs in the CdC_8 matrix was 4 mol. %. The concentration of C QDs in the CdC_8 matrix was 2 wt %. Thus, when the two types of QDs were combined in the CdC_8 matrix, the concentration of CdS QDs was 4 mol. % and the concentration of C QDs was 2 wt % concurrently.

3. Results and discussion

3.1. Raman microscopy

Raman spectroscopy was used to analyze the CdC_8 matrix to study the molecular vibrations and structural properties of the material (Fig. 2). This method provides information about the vibrational modes of molecules and intermolecular interactions. It is particularly important for the design of nanocomposites based on organic matrices.

The micro-Raman analysis was performed at room temperature in a backscattering geometry using two Raman spectrometers – a Witec 300 alpha R setup with a spectral resolution of ≈ 1.0 cm^{-1} and a Renishaw inVia Reflex spectrometer with a spectral resolution of ≈1.6 cm^{-1}. The 532 nm laser was used as the illumination source. Zeiss LD EC Epiplan-Neofluar 50 × /0.55 (Witec) and Leica N PLAN EPI 50 × /0.75 (Renishaw) objectives were used. The lateral resolutions of these lenses were ≈0.6 μm (Witec) and ≈ 0.45 μm (Renishaw). A laser power of $\lesssim$ 5 mW was selected at the back of the objective. The edge filters were utilized to separate the Raman signal from the excitation line. The edge filters had a cutoff of 90 cm^{-1} (Witec) and 100 cm^{-1} (Renishaw). We used a 1600 × 200 pixel Newton Andor EMCCD camera as the detector (for the Witec setup) and a 1024 × 256 pixel Renishaw Centrus CCD detector (for the Renishaw setup).

Raman scattering mapping was performed on the CdC_8 matrix surface with an area of 50 × 50 μm^2 using the 100 × 100 pixel scan. The Raman spectrum of the CdC_8 matrix is analyzed in detail below.

The molecular vibrations in the CdC_8 matrix are described in Table 1. The analysis of these data allows us to gain an understanding of the chemical bonds and functional groups in the CdC_8 matrix, which is important for studying the properties of new nanocomposites. Each peak in the table reflects the interactions and arrangement of the atoms in the molecule and is associated with a particular type of movement.

3.2. Optical spectroscopy

The spectral characteristics of the CdC_8 matrix-based nanocomposites were studied using a Denovix DS-11-FX spectrometer, which

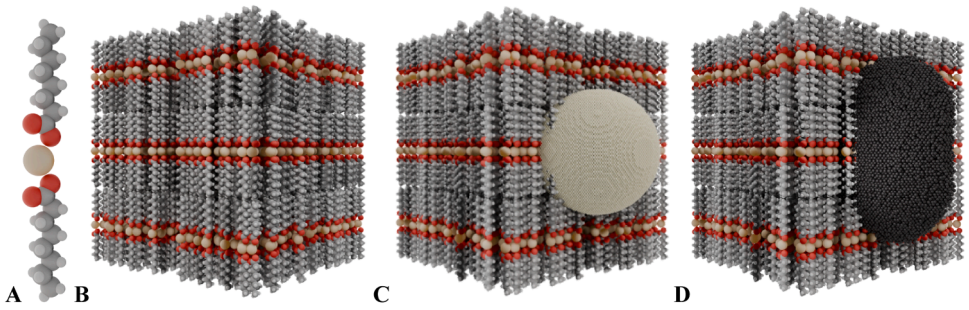

Fig. 1. Schematic presentations of: **A.** The three-dimensional structure of the CdC_8 molecule consisting of a central cadmium ion (Cd^{2+}, large diameter ion) coordinated by two octanoate anions ($C_7H_{15}COO^-$). The carbon atoms are shown in gray, hydrogen atoms in white, and oxygen atoms in red. **B.** The three-dimensional structure of the CdC_8 matrix, displaying the arrangement of the ILC molecules in smectic A structure. **C.** The CdC_8 matrix containing the synthesized CdS QDs. **D.** The CdC_8 matrix containing synthesized C QDs.

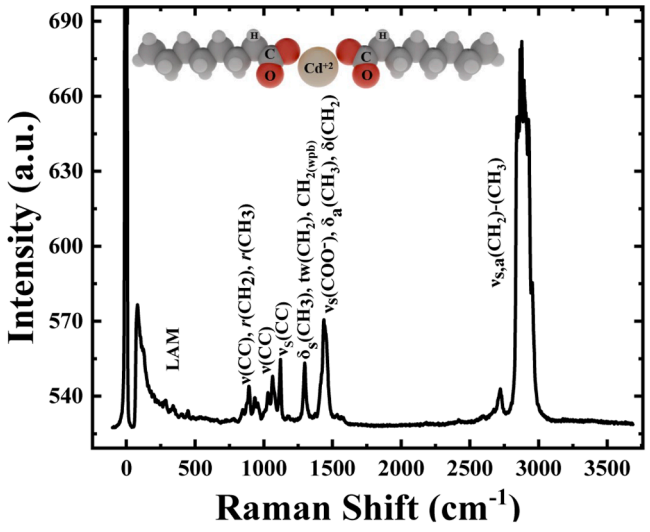

Fig. 2. Raman spectroscopy provides the information about molecular vibrations in the CdC_8 matrix, which is important for studying the properties of new nanocomposites.

Table 1
The characteristic vibrational wave numbers (cm^{-1}) observed for the CdC_8 matrix.

Symbol	Description	Frequency (cm^{-1})
$\nu_a(CH_3)$	Asymmetric stretching of the methyl group	2950–2970
$\nu_a(CH_2)$	Asymmetric stretching of methylene groups	2915–2935
$\nu_a(CH_2)_{Fermi\ res.}$	Asymmetric stretching of methylene groups with Fermi resonance	2885–2890
$\nu_s(CH_2)$, $\nu_a(CH_2)$	Symmetric and asymmetric stretching of the methylene groups	2840–2860
$\nu_s(COO^-)$, $\delta_a(CH_3)$, $\delta(CH_2)$	Symmetrical stretching of the carboxylate group. Asymmetric deformation vibrations of methyl groups. Deformation vibrations of methylene groups.	1390–1500
$\delta_s(CH_3)$, $tw(CH_2)$, $CH_{2(wpb)}$	Symmetric deformation vibrations of methyl group. Twist vibrations of methylene groups. Wagging progression bands vibrations of methylene groups.	Around 1300
$\nu_s(CC)_{all\text{-}trans}$	Symmetric stretching of the carbon–carbon bond in molecules with a straight configuration	1120–1130
$\nu(CC)$	Valence vibrations of the carbon–carbon double bond	Around 1060 and 890
$r(CH_3)$	Rocking vibration of the methyl group	Around 940
$r(CH_2)$	Rocking vibration of the methylene group	Around 850
LAM	Lattice acoustic mode (lattice vibrations)	90–450

enables measurements of optical spectra in the range from 190 nm to 850 nm. This method is highly sensitive, but requires samples to be in the liquid state. The nanocomposites were therefore dissolved in hexane (C_6H_{14}), which prevents the QDs from stacking together after dissolution. The measurements were carried out in a quartz cuvette with a 1 cm path length. This ensured material stability and enabled accurate spectral data to be obtained. Optical spectra measured in the UV and visible range display the absorption characteristics of CdS QDs, C QDs, and a combination of both (Fig. 3). The absorption maximum of CdS QDs is registered in the range from 305 nm to 340 nm, reaching a maximum at 322 nm. This narrow absorption maximum indicates the low dispersion of the CdS QDs and the non-aggregation of the CdS QDs, which reflects the high quality of the synthesized composites. It should be noted that for pure CdS, the absorption spectrum of bulk hexagonal CdS is observed

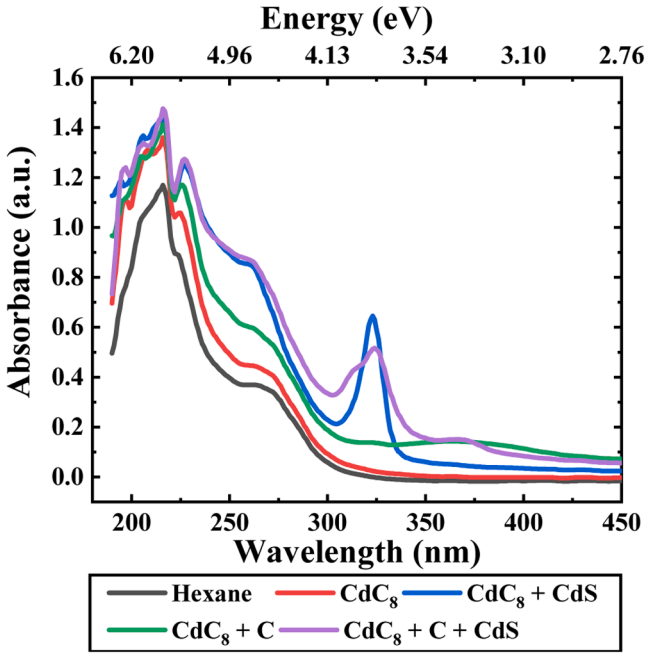

Fig. 3. Absorption spectra of nanocomposites, obtained from the CdC_8 matrix with QDs. Liquid samples are prepared by diluting the nanocomposite materials in hexane. The black line represents the spectrum measured for pure hexane. The red line represents the spectrum of the pure CdC_8 matrix (7.5 mg) dissolved in hexane (1 ml). The blue line shows the spectrum of the CdC_8 + CdS QDs matrix (20 mg) dissolved in hexane (15 ml). The green line depicts the spectrum of the CdC_8 + *C* QDs matrix (8.5 mg) dissolved in hexane (3 ml). The purple line depicts the spectrum of the CdC_8 + CdS QDs + *C* QDs matrix (13.5 mg) dissolved in hexane (6 ml). In all measurements a path length of absorbing media is 1 cm.

at a wavelength of 512 nm. Such a strong change in the absorption spectrum down to 325 nm can be explained as the result of quantization effects occurring in the transition from macroscopic samples to nanoscale materials.

C QDs have a broad absorption maximum, registered in the range from 335 nm to 415 nm with a maximum at 380 nm. For the nanocomposite in which both CdS QDs and C QDs were synthesized, the onset of the spectrum was slightly changed. This can be explained by the interaction between different types of CdS QDs and C QDs. Such interactions between the QDs can affect the electron levels and introduce changes in the absorption spectrum compared to the spectra registered for pure CdS QD and C QD samples. In the case of combined CdS QDs and C QDs, the absorption spectrum for CdS QDs is found in the range from 305 nm to 355 nm with a maximum at 322 nm, while for C QDs the absorption spectrum ranges from 355 nm to about 390 nm with a maximum at 368 nm.

To analyze the effect of temperature changes on the optical properties of CdS QDs, which is important for their application in temperature sensors and optoelectronic devices, the absorption maximum of CdS QDs were measured at different temperatures (Fig. 4): 20 °C, 50 °C, 70 °C, 80 °C, 90 °C, 100 °C, and 110 °C. This allowed us to analyze the shift of the absorption maximum from 322 nm to 333 nm.

Change in absorption from 322 nm to 333 nm can be caused by several factors. Firstly, as the temperature increases, the thermal motion energy of the atoms increases. This increases the lattice vibrations and thus changes the energy structure of the CdS QDs, which can be measured as a change in the wavelength of light absorption. Secondly, temperature changes affect intermolecular interactions, such as the bond strength between the QDs and the CdC_8 matrix. This affects the shift of the absorption maximum. The study of temperature dependence provides an understanding of CdS QDs behavior under different conditions and their potential applications in optoelectronic devices.

We used the Tauc plot [33] to accurately determine the band gap of CdS QDs instead of using the wavelength of maximum absorption because this wavelength does not always precisely reflect the band gap, especially for nanomaterials [34]. In CdS QDs, the band gap changes due to quantization effects, and measurement based only on the absorption wavelength may result in underestimation of the band gap. The following equation can be used for the Tauc plot:

$$(ahv)^n = A(hv - E_{gap}) \quad (1)$$

where a is the absorption coefficient, hv is the photon energy (where h is Planck's constant and v is the frequency of light), A is an energy independent constant, E_{gap} is the band gap width, and n is a parameter that depends on the type of transition in the material ($n = 1/2$ for direct band gap, $n = 2$ for indirect band gap).

We used $n = 1/2$ in the Tauc plot equation because CdS is a material with a direct band gap transition. Using the Tauc plot (Fig. 5) and analyzing its linear part allows us to precisely determine the band gap for CdS QDs, which is especially important for evaluating the changes in band gap at different temperatures.

The band gap value is the intersection of the extrapolation of the linear section with the hv axis. The band gaps of the CdS QDs were: 3.63 eV, 3.62 eV, 3.61 eV, 3.59 eV, 3.58 eV, 3.58 eV, 3.56 eV for temperatures: 20 °C, 50 °C, 70 °C, 80 °C, 90 °C, 100 °C, 110 °C, respectively. The band gaps of CdS QDs are used to estimate the diameter of the spherical CdS QDs. From the difference in band gap energies and the material factor, the diameter of CdS QDs was calculated (Fig. 6) using Bruce's equation [35]:

$$E_{\text{gapQD}} = E_{\text{gapB}} + \frac{h^2}{8R^2}\left(\frac{1}{m_e^*} + \frac{1}{m_h^*}\right) - \frac{1.8e^2}{4\pi\varepsilon_0\varepsilon_r R} \quad (2)$$

where E_{gapQD} is the band gap of the QD; E_{gapB} is the band gap of the bulk material; R is the radius of the QD; h is the Planck's constant; m_e^* is the effective mass of the electron in the QD; m^*_h is the effective mass of the hole in the QD; 1.8 is the empirical coefficient accounting for the Coulomb interaction between the electron and the hole; e is the elementary charge ($e = 1.602 \times 10^{-19}$C); ε_0 is the vacuum permittivity; and ε_r is the relative permittivity of the QD material.

We have used the Brus equation for the theoretical estimation of the CdS QDs diameter both for the simple model (black line) and model considering the Coulomb interaction (red line), using the following material parameters for CdS: dielectric constant $\varepsilon_r = 9$, bulk band gap energy $E_{gapB} = 2.42$ eV, effective hole mass $m^*_h = 0.8m_0$, and effective electron mass $m_e^* = 0.21m_0$, where $m_0 = 9.11 \times 10^{-31}$ kg is the free

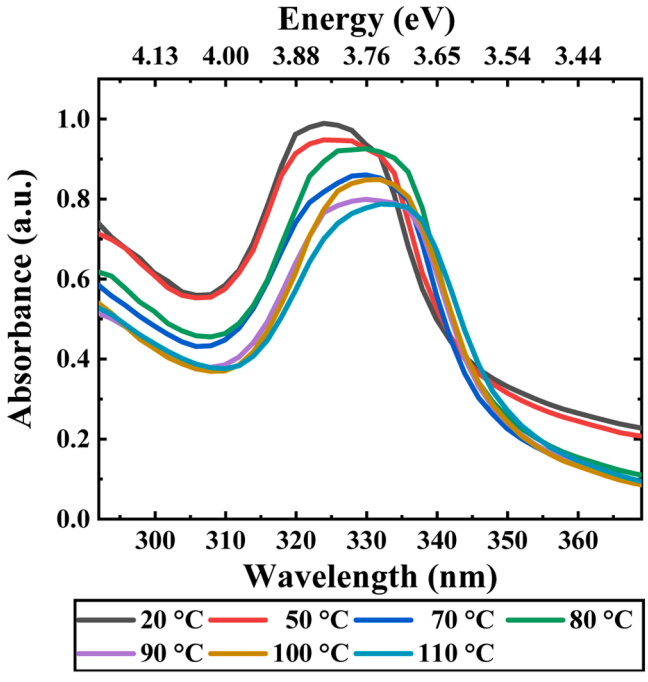

Fig. 4. Change in the absorption maximum position of CdS QDs with increasing temperature from 20 °C to 110 °C, demonstrating shift from 322 nm to 333 nm.

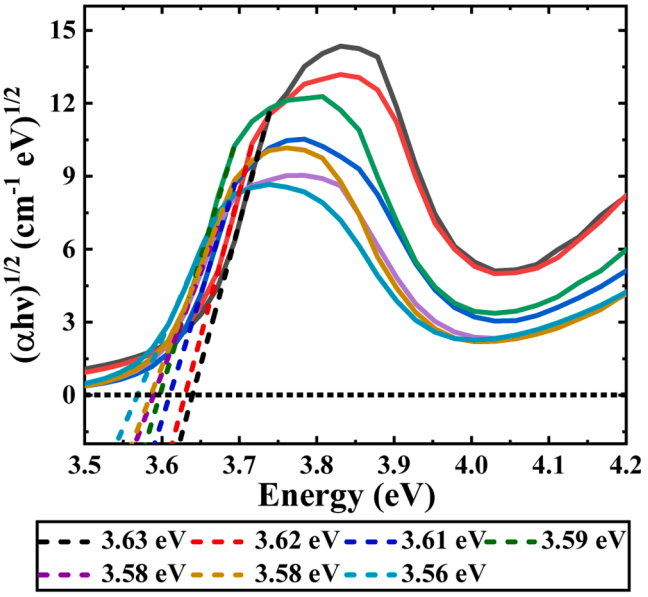

Fig. 5. Tauc plot for CdS QDs, displaying the calculation of the band gap energy with increasing temperature from 20 °C to 110 °C, derived from absorbance data using $(ahv)^{1/2}$ as a function of photon energy hv. The curves are color-coded: 20 °C (black), 50 °C (red), 70 °C (blue), 80 °C (green), 90 °C (pink), 100 °C (brown), and 110 °C (cyan).

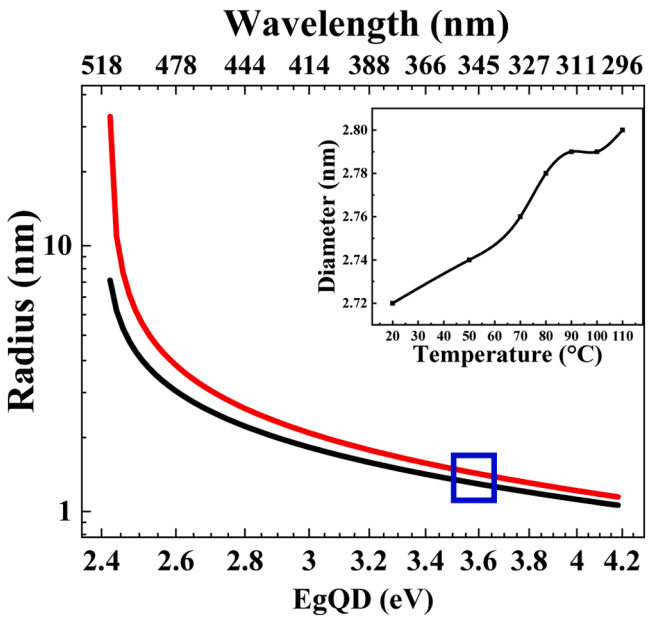

Fig. 6. Theoretical dependence of the CdS QDs diameter on the band gap energy, calculated using the Brus Eq. (2): simple model (black line) and model considering Coulomb interaction (red line). The area corresponding to the band gap values obtained by the Tauc method is indicated by the blue rectangle. The inset shows the theoretically derived diameters of CdS QDs as a function of temperature.

electron rest mass. These parameters were used to plot the dependence of the radius on the band gap energy of CdS QDs, determined by the Tauc method. The area corresponding to the band gaps obtained by the Tauc method is indicated by the blue rectangle. The inset shows the diameter of the CdS QDs as a function of temperature, derived from the data shown in Fig. 6.

The diameter, estimated using Bruce's equation, for CdS QDs is found to be in the range from 2.7 nm to 2.8 nm, corresponding to the temperature range from 20 °C to 110 °C. The change in size can be explained considering several of factors. One of them is the thermal expansion of CdS QDs at higher temperatures [36]. The interaction between the CdC_8 matrix and the CdS QDs, causing additional stretching of the latter, is another potential factor. Changes in temperature can affect the physical and chemical properties of the CdC_8 matrix [37], resulting in thermal expansion. This, in turn, can result in a slight stretching of the CdS QDs, which contributes to their increase in size with increasing temperature.

The calculated sizes of CdS QDs using Bruce's equation are in good agreement with the results from TEM studies shown in Fig. 7a, which gave the value of 2.48 nm. At the same time, the Bruce equation cannot be applied for C QDs due to their flaky nature. Furthermore, we have no information on the parameters of the synthesized C QDs, such as dielectric constant, band gap energy, electron and hole masses, which can vary significantly depending on the type of C. For example, for graphene, typical values are: $\varepsilon_r \approx 2.5$, $E_{gapB} \approx 0$ eV, $m^*_h \approx 0.01m_0$, $m_e \approx 0.01m_0$ [38,39]. On the other hand, for the most insulating forms of carbon, such as amorphous carbon, the parameters can be: $\varepsilon_r \approx 4$, $E_{gapB} \approx 2.2$ eV, $m^*_h \approx 0.5m_0$, $m^*_e \approx 0.5m_0$ [40,41]. Their characteristic diameters were measured using TEM (see Fig. 7d below). The diameter is found to be in the range from 6 nm to 10.5 nm.

3.3. Characteristic sizes of QDs studied using TEM

To analyze the samples, we used the FEI Titan Tecnai G2 F20 TEM, equipped with a Gatan Tridiem 863P post-column image filter (GIF) and a high-angle energy-dispersive X-ray (EDX) detector. To study the sizes of CdS QDs and C QDs, we dissolved the CdC_8 + CdS and CdC_8 + *C* nanocomposites in hexane - C_6H_{14}. Subsequently, 1 μl of the obtained substance was dropped onto the top of the ultrathin carbon film-supported copper grid for TEM analysis and was then allowed to evaporate in hexane under a ventilation hood.

Fig. 7a shows the TEM images for the CdS QDs and Fig. 7c shows the results for the C QDs obtained by TEM. Some atom planes are highlighted via yellow lines on the high-resolution TEM image (Fig. 7a). The fast Fourier transform (Fig. 7a, inset images) reveals the crystalline nature of the CdS QDs regions and represents the corresponding atom planes orientation in the reciprocal space. d-spacing, calculated for regions 1–3 on the image, is in perfect agreement with crystallography data for CdS. Specifically, the atomic layer distances are 0.28 nm for region 1, 0.34 nm for region 2, and 0.35 nm for region 3. Additionally, we performed Miller index matching for these planes, confirming the hexagonal structure of the CdS QDs. The results show a (4,5,1) orientation for region 1 with a 99.96 % match, a (0,6,1) orientation for region 2 with a 99.53 % match, and a (4,4,0) orientation for region 3 with a 98.76 % match. The size analysis of CdS QDs and C QDs from TEM images was performed using ImageJ software [42]. The results of the size distribution for CdS QDs and C QDs are shown in Fig. 7b and Fig. 7d respectively.

The size of the CdS QDs ranges from about 1.9 nm to 3.7 nm. The mode diameter of the synthesized CdS QDs was estimated to be 2.48 nm with a standard deviation of 0.26 nm, as determined from Gaussian fitting of the size distribution data, indicating a high degree of monodispersity. The characteristic size distribution of the C QDs ranged from 6 nm to 10.5 nm, with a mode diameter of 8.23 nm and a standard deviation of 1.41 nm, as determined from Gaussian fitting of the size distribution data. This indicates a high degree of control over the synthesis process, which resulted in a low size dispersion of the QDs. It should be noted that the characteristic dimension used to describe the C QDs is in a range that correlates with the characteristic diameter, which is calculated as the diameter of a circle whose area is equal to the area of the C QDs. This approach is suitable, since the C QDs have a non-spherical shape and their dimensions cannot be accurately described by the length or width of the C QDs itself.

3.4. Photovoltaic properties

We investigated the photovoltaic properties of the pure CdC_8 matrix, the nanocomposites CdC_8 + CdS QDs and CdC_8 + C QDs, as well as a combination of CdC_8 + CdS QDs + C QDs (Figure 8). Merck ITO glass slides with a sheet resistance of 15-25 Ω/ were used for sample preparation. The slides were cleaned with acetone, isopropanol, and Milli-Q water in turn as a part of the preparation process. ILC powder with different types of QDs was deposited on the surface of the ITO glass. To define the sample thickness, 50 μm spacers were positioned at four corners of a rectangular shaped glass. Samples were then heated to 130°C. As a result of the heating, the ILC powder melted. Next, the second piece of glass was placed on the top to form the sandwich cell, containing the nanocomposite material. After cooling down to room temperature, glassy nanocomposites with different types of QDs were obtained. The working electrode has an area of 1 cm^2. The smectic layers of the samples under investigation were oriented parallel to the substrates. The top electrode was illuminated and connected to the positive terminal. A high-precision Keithley 2635B source meter, a Hamamatsu 200 series L7212 ultraviolet (UV) light source with an L7212-02 lamp and a wavelength from 240 nm to 400 nm were used to determine the photovoltaic properties of the samples. Samples were placed at a distance of 40 cm from the UV light source to prevent the heat affecting the experiment. Lamp irradiance was measured using a Thorlabs PM100D power meter with a Thorlabs S401C sensor at the sample location and was found to be 1.5 mW/cm^2 at a distance of 40 cm from the light source.

The dynamics of the photovoltaic response in the short-circuit

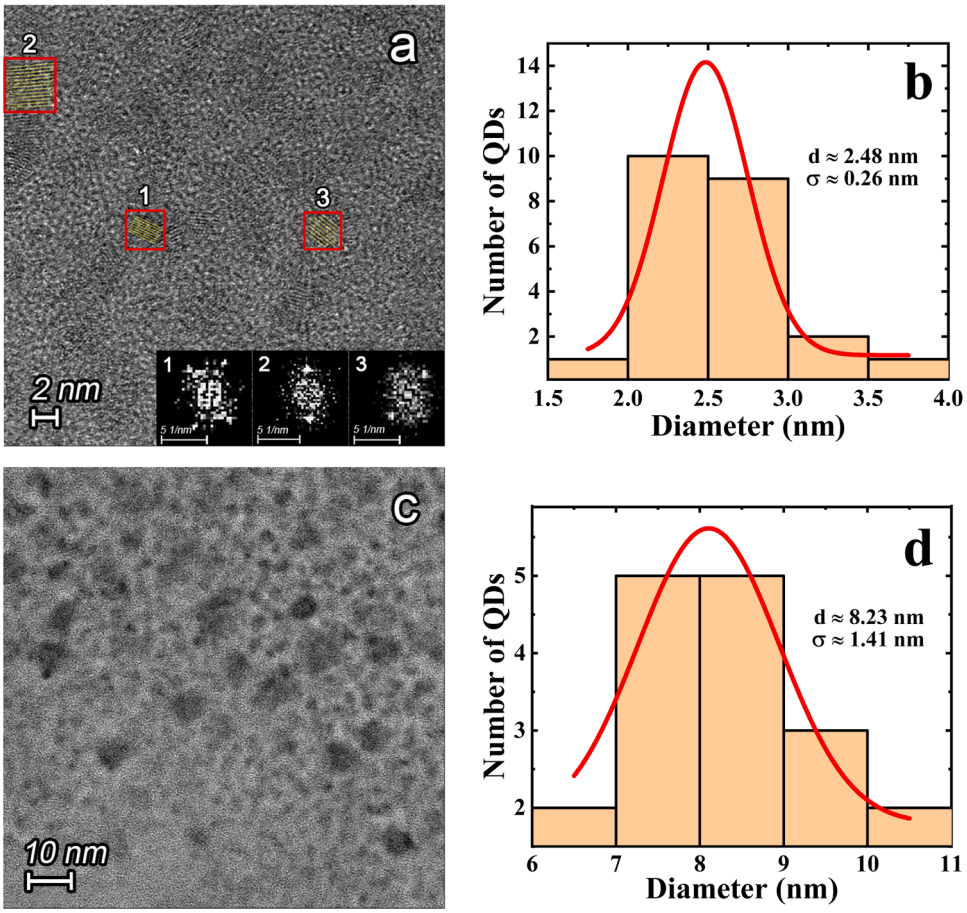

Fig. 7. a. TEM image of CdC_8 matrix with CdS QDs. The image is provided with the atomic planes marked by yellow lines. The insets display the fast Fourier transform of the rectangular regions marked with red frames. **b.** The histogram reflecting the diameter distribution of the CdS QDs data and the Gaussian fitting of the data. **c.** TEM image for CdC_8 matrix with C QDs. **d.** The histogram reflecting the diameter distribution of the C QDs data and the Gaussian fitting of the data.

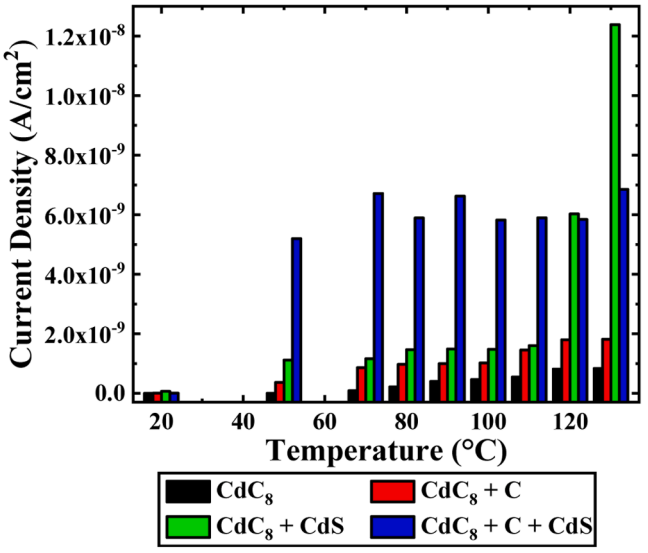

Fig. 8. Photovoltaic properties of the pure CdC_8 matrix (black bars), CdC_8 + *C* QDs (red bars), CdC_8 + CdS QDs (green bars), and a combination of CdC_8 + CdS QDs + *C* QDs (blue bars).

current configuration was recorded using the «timetrace» technique, with the light pulse duration of 15 s, followed by 60 s relaxation in dark. The photoelectric current in the nanocomposites was determined by the averaging during the irradiation with UV light.

The mechanisms of photovoltaic current generation in nanocomposites can be described by considering the Dember effect [43,44]. The Dember effect describes the generation of an electric field resulting from the difference in the mobility of electrons (μ_n) and holes (μ_p) under the conditions of a carrier concentration gradient. Estimations in [45] show that the maximum value of the electromotive force for the Dember effect can reach 0.5 V. This value is sufficient to provide the short circuit current registered in our experiments. The Dember voltage can be described using the following equation:

$$U = G_0 \frac{k_B T}{e} \frac{\mu_n - \mu_p}{n\mu_n - p\mu_p} \frac{1}{\sqrt{\frac{D}{\tau} + s}} \quad (3)$$

where G_0 is the surface density of photons; k_B is the Boltzmann constant; T is the absolute temperature; e is the charge of the electron; D is the ambipolar diffusion coefficient; τ is the lifetime of charge carriers; s is the magnitude of the surface recombination of charge carriers; and n and p are the concentrations of negative and positive charges, respectively.

For the pure CdC_8 matrix, the photocurrent shows the lowest values for all the samples, increasing from 6.0×10^{-13} A/cm^2 at 20 °C to 8.3×10^{-10} A/cm^2 at 130 °C. This is an indication of the low photovoltaic activity in the material. The CdC_8 matrix is characterized by a smectic A structure with ionic conductivity. In this case, the structure provides ordered layers of molecules, which allow for a charge transfer through the CdC_8 matrix. However, its efficiency is limited by the low mobility of the charge carriers in a perpendicular direction to the smectic layers, as the arrow in Fig. 9 points.

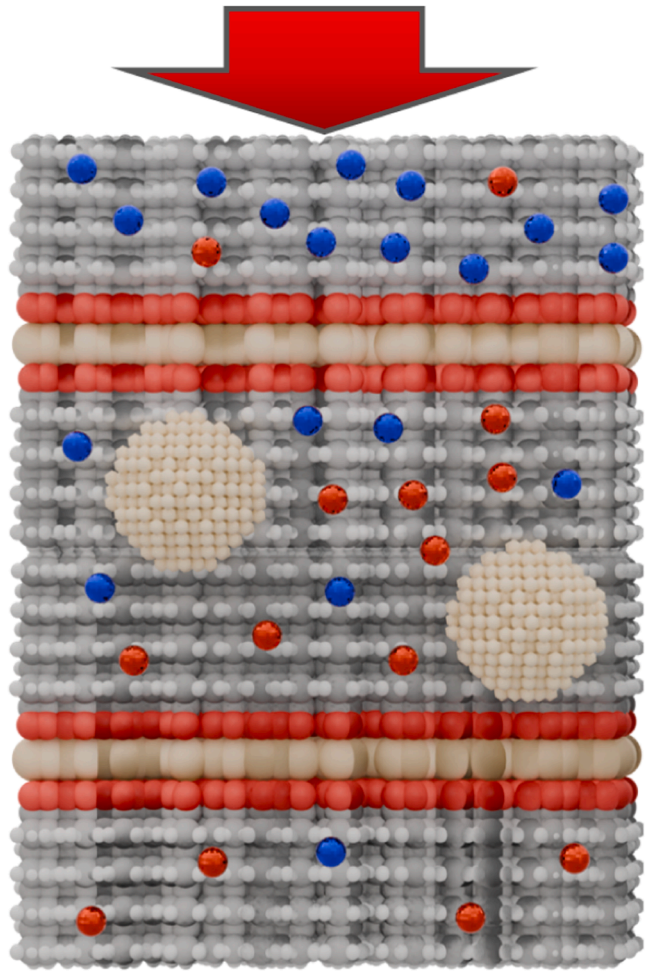

Fig. 9. The schematic image demonstrates the photoconductivity effect in nanocomposites with a layered ILC CdC_8 structure due to the Dember effect. The small red dots depict holes, whilst the small blue dots depict electrons. The large sand-colored circles represent CdS QDs. The red arrow points in the direction of the applied UV light, illustrating the interaction of the nanocomposite with UV irradiation and the movement of charge carriers.

The generation of electron–hole pairs by absorbing UV radiation in the CdC_8 matrix molecules is the main mechanism of photocurrent generation. However, in the absence of QDs, charge recombination processes remain dominant. This means that the CdC_8 matrix has insufficient transport properties despite the formation of charge carriers. The charges (electrons and holes) do not move efficiently in the volume of the material and recombine rapidly. This process results in a significant reduction in the photocurrent and a decrease in the overall efficiency of the power conversion process.

For the CdC_8 + *C* QDs nanocomposite, an increase in photocurrent is observed starting from 4.2×10^{-12} A/cm^2 at 20 °C and rising up to 1.8×10^{-9} A/cm^2 at 130 °C. This indicates an enhanced photovoltaic effect due to C QDs, which results in the formation of additional states in the energy structure of the CdC_8 matrix. This causes the increased absorption of photons, which causes more charged carriers to be generated [46,47]. The formation of additional transport pathways and the reduction of recombination due to the reduced interaction of charges with the surface states of C QDs is in good agreement with the main mechanism of photocurrent enhancement [48]. The probability of recombination at the surface states on the C QDs decreases due to the increased mobility of charged carrier transport to the electrodes. Compared to a pure CdC_8 matrix, electrons move faster than holes in CdS_8 + *C* QDs nanocomposite material, enhancing the manifestation of the Dember effect. The quantum-size effect due to the reduced size of C QDs results in the increased probability of interlevel transitions with an energy of ≈3.5 eV, which enhances the generation of electron–hole pairs. As a result, the charge separation in the CdC_8 matrix became more effective. This enhances the local Dember electric field, resulting in an increase of the photovoltaic current. It should be emphasized that C QDs have high chemical and photostability. This ensures stable operation under light irradiation.

The photocurrent of the CdC_8 + CdS QDs nanocomposite material is even higher than that of the C QDs sample. The magnitudes increase from 6.5×10^{-11} A/cm^2 at 20 °C to 1.2×10^{-8} A/cm^2 at 130 °C, indicating more efficient carrier separation and conduction than in the CdC_8 + *C* QDs nanocomposite. The CdS QDs material absorbs photons in the UV region corresponding to their band gap energy (≈3.6 eV), generating more electron–hole pairs. The surface of CdS QDs promotes the efficient separation of electrons and holes, preventing recombination [49,50]. The electrons in CdS QDs have a high mobility, which results in a large difference in the mobility of electrons and holes, resulting in the manifestation of a strong Dember effect.

The most significant response is observed for the CdC_8 + *C* QDs + CdS QDs nanocomposite: current changes starting from 5.0×10^{-12} A/cm^2 at 20 °C and was increasing up to 6.9×10^{-9} A/cm^2 at 130 °C. The combination of C QDs + CdS QDs creates a synergistic effect that enhances the generation and transport of photo-charges, which can already be detected at 50 °C. C QDs + CdS QDs extend the UV absorption spectrum with an absorption maximum for C QDs at 368 nm (≈3.5 eV) and CdS QDs at 325 nm (≈3.85 eV), increasing the total number of photons absorbed. The high electron mobility on the surface of CdS QDs promotes efficient electron–hole separation, which enhances the Dember effect in the nanocomposite material. C QDs support the formation of additional charge transfer pathways in the CdC_8 matrix and reduce the recombination due to reduced charge interactions with the surface states of the C QDs.

Thus, the addition of both C QDs and CdS QDs enhances the charge absorption, generation, and transport processes and improves the photovoltaic response. The combination of C QDs + CdS QDs in the CdC_8 matrix produces the best results due to the broadened absorption spectrum and the optimized carrier separation. It should be emphasized, that in the CdC_8 matrix, containing both C QDs and CdS QDs, high current values are registered. The mechanism of photovoltaic current excitation is explained by considering of the Dember effect, where the electric field is generated due to the difference in mobility of electrons and holes. This results in photocurrent enhancement. In addition, the introduction of C QDs and CdS QDs into the CdC_8 matrix increases the carrier concentration and assists in the formation of additional charge transfer pathways due to the QDs. This improves charge transport and reduces charge recombination. Thus, the addition of C QDs and CdS QDs improves the photovoltaic response by optimizing the absorption, generation, and charge transport processes.

4. Conclusions

The Raman spectrum of the CdC_8 matrix, which was previously missing, was studied to characterize molecular vibrations and identify the features of chemical bonds and functional groups. A narrow absorption maximum at 322 nm was observed during the spectral characterization of the nanocomposites with CdS QDs, synthesized basing on the CdC_8 matrix. These spectral data demonstrate low dispersion and no aggregation of the CdS QDs. A broader absorption maximum centered at 380 nm was registered for nanocomposites with C QDs. For the nanocomposite including both CdS QDs + *C* QDs, the absorption spectrum demonstrates both maximums at 324 nm for CdS QDs and 368 nm for C QDs, indicating an interaction between the two types of QDs. The energy band gap of the CdS QDs is determined, using the Tauc method, to be about 3.6 eV. This approach allowed us to accurately determine the energy value at which a sharp increase in absorption occurs, indicating

the transition of electrons from the valence band to the conduction band. The dimensional changes of CdS QDs, caused by increasing temperature, are estimated using the Bruce equation. Theoretical estimations show that the diameter of CdS QDs increases from 2.7 nm to 2.8 nm when the nanocomposite material is heated from 20 °C to 110 °C. The effect can be explained by the thermal expansion of the CdS QDs and changes in the interaction of the CdS QDs with the CdC_8 matrix upon heating. The theoretically obtained values are in good agreement with the results of TEM studies, which confirm that the dimensions of the CdS QDs are estimated to be about 2.5 nm. The results of our studies of nanocomposite materials have shown that the addition of CdS QDs and C QDs to the CdC_8 matrix improves the photovoltaic properties of the material due to the Dember effect. The largest photocurrent was observed in the CdC_8 matrix with the combination of C QDs + CdS QDs, indicating a synergistic effect between the two types of QDs resulting in an optimized photovoltaic response. These novel nanocomposite materials open new horizons for the development of high-precision sensors and optoelectronic devices, which can be used in various application fields, including solar power industry and optoelectronics. The developed materials have significant potential for the creation of efficient and high-resolution devices, which lead to significant improvements in technologies and commercialization of advanced solutions.

CRediT authorship contribution statement

D. Zhulai: Writing – review & editing, Writing – original draft, Visualization, Validation, Supervision, Software, Project administration, Investigation. **N. Boichuk:** Writing – review & editing, Validation, Software, Methodology, Formal analysis. **D. Pustovyi:** Investigation. **G. Beltramo:** Investigation. **O. Kovalchuk:** Writing – review & editing. **Y. Garbovskiy:** Writing – review & editing. **G. Klimusheva:** Writing – review & editing, Methodology. **G. Yaremchuk:** Methodology, Investigation. **T. Mirnaya:** Writing – review & editing, Methodology, Investigation. **S. Vitusevich:** Writing – review & editing, Supervision, Project administration, Formal analysis, Data curation, Conceptualization.

Declaration of competing interest

The authors declare that they have no known competing financial interests or personal relationships that could have appeared to influence the work reported in this paper.

Acknowledgments

D. Zhulai is grateful for a research grant received from the German National Academy of Sciences Leopoldina. The authors would also like to acknowledge funding from NASU via project No 0123U100832. TEM experimental data are obtained *at the Ernst Ruska-Centre (ER-C) for Microscopy and Spectroscopy with Electrons at the Forschungszentrum Jülich (FZJ) in Germany*. The ER-C beam-time access was provided via the Transnational Access in the frame of ESTEEM3 Project, the funding from European Union's Horizon 2020 Research and Innovation Programme (Grant No 823717, project "ESTEEM3").

Data availability

Data will be made available on request.

References

[1] Yan Fei, et al., Light generation in lead halide perovskite nanocrystals: lEDs, color converters, lasers, and other applications, Small 15 (47) (2019) 1902079, https://doi.org/10.1002/smll.201902079.
[2] Sivis Murat, et al., Extreme-ultraviolet light generation in plasmonic nanostructures, Nat. Phys. 9 (5) (2013) 304–309, https://doi.org/10.1038/nphys2590.
[3] C. Forsythe Ryland, et al., Pulsed laser in liquids made nanomaterials for catalysis, Chem. Rev. 121 (13) (2021) 7568–7637, https://doi.org/10.1021/acs.chemrev.0c01069.
[4] Luo Xiongfei, et al., Light-mediated polymerization catalyzed by carbon nanomaterials, Angew. Chem. Int. Ed. 63 (18) (2024) e202316431, https://doi.org/10.1002/anie.202316431.
[5] Zhao Xiaoli, et al., Integration and applications of nanomaterials for ultrafast photonics, Laser. Photon. Rev. 16 (11) (2022) 2200386, https://doi.org/10.1002/lpor.202200386.
[6] Thakur Abhinay, Ashish Kumar, Recent advances on rapid detection and remediation of environmental pollutants utilizing nanomaterials-based (bio) sensors, Sci. Total. Environ. 834 (2022) 155219, https://doi.org/10.1016/j.scitotenv.2022.155219.
[7] A. Triana Manuel, et al., Luminescent nanomaterials for energy-efficient display and healthcare, ACS. Energy Lett. 7 (3) (2022) 1001–1020, https://doi.org/10.1021/acsenergylett.1c02745.
[8] Rohilla Deepak, Savita Chaudhary, Ahmad Umar, An overview of advanced nanomaterials for sensor applications, Eng. Sci. 16 (2021) 47–70, https://doi.org/10.30919/es8d552.
[9] K.S. Poon Joyce, et al., Silicon photonics for the visible and near-infrared spectrum, Adv. Opt. Photonics. 16 (1) (2024) 1–59, https://doi.org/10.1364/AOP.501846.
[10] Zhi-Xiang Zhang, et al., High-performance flexible GaAs nanofilm uv photodetectors, ACS. Appl. Nano Mater. 6 (11) (2023) 9917–9927, https://doi.org/10.1021/acsanm.3c01875.
[11] Sharma Ram Chhavi, et al., Gallium arsenide and gallium nitride semiconductors for power and optoelectronics devices applications, Conf. Ser. Vol 2426 (1) (2023), https://doi.org/10.1088/1742-6596/2426/1/012008. IOP Publishing.
[12] A. Steiner Myles, et al., High efficiency inverted GaAs and GaInP/GaAs solar cells with strain-balanced GaInAs/GaAsP quantum wells, Adv. Energy Mater. 11 (4) (2021) 2002874, https://doi.org/10.1002/aenm.202002874.
[13] Zumeit Ayoub, et al., Printed GaAs microstructures-based flexible high-performance broadband photodetectors, Adv. Mater. Technol. 7 (12) (2022) 2200772, https://doi.org/10.1002/admt.202200772.
[14] Kambhampati Patanjali, Nanoparticles, nanocrystals, and quantum dots: what are the implications of size in colloidal nanoscale materials? J. Phys. Chem. Lett. 12 (20) (2021) 4769–4779, https://doi.org/10.1021/acs.jpclett.1c00754.
[15] Hassan Tufail, et al., Functional nanocomposites and their potential applications: a review, J. Polym. Res. 28 (2) (2021) 36, https://doi.org/10.1007/s10965-021-02408-1.
[16] García de Arquer F. Pelayo, et al., Semiconductor quantum dots: technological progress and future challenges, Science 373 (6555) (2021) eaaz8541, https://doi.org/10.1126/science.aaz8541.
[17] Baig Nadeem, Irshad Kammakakam, Wail Falath, Nanomaterials: a review of synthesis methods, properties, recent progress, and challenges, Mater. Adv. 2 (6) (2021) 1821–1871, https://doi.org/10.1039/D0MA00807A.
[18] A. Altammar Khadijah, A review on nanoparticles: characteristics, synthesis, applications, and challenges, Front. Microbiol. 14 (2023) 1155622, https://doi.org/10.3389/fmicb.2023.1155622.
[19] Kuan-Ju Wu, et al., CdS nanorods imbedded in liquid crystal cells for smart optoelectronic devices, Nano Lett. 7 (7) (2007) 1908–1913, https://doi.org/10.1021/nl070541n.
[20] G. Singh, S. Kumar, et al., Recent trends and insights into carbon dots dispersed liquid crystal composites, J. Mol. Liq. 384 (2023) 122225, https://doi.org/10.1016/j.molliq.2023.122225.
[21] Karel Goossens, et al., Ionic liquid crystals: versatile materials, Chem. Rev. 116 (8) (2016) 4643–4807, https://doi.org/10.1021/cr400334b.
[22] Nadia Kapernaum, et al., Current topics in ionic liquid crystals, Chempluschem 87 (1) (2022) e202100397, https://doi.org/10.1002/cplu.202100397.
[23] R. Pratibha, W. Park, et al., Colloidal gold nanosphere dispersions in smectic liquid crystals and thin nanoparticle-decorated smectic films, J. Appl. Phys. 107 (6) (2010), https://doi.org/10.1063/1.3330678.
[24] T. Mirnaya, et al., Synthesis and optical properties of liquid crystalline nanocomposites of cadmium octanoate with CdS quantum dots, Phys. Chem. Solid State 13 (2012) 131–135.
[25] Rudenko Valentyn, et al., Modifying optical nonlinearities of ionic liquid crystal glass by adding gold and carbon nanoparticles, J. Mol. Liq. 393 (2024) 123641, https://doi.org/10.1016/j.molliq.2023.123641.
[26] Rudenko Valentyn, et al., Tuning Effective Optical Nonlinearities of Overlooked Glass-Forming Ionic Liquid Crystals, Optica Publishing Group, 2024, https://doi.org/10.1364/NOMA.2024.NoTh1G.5. Novel Optical Materials and Applications.
[27] Valentyn Rudenko, et al., Exploring optical nonlinearities of glass nanocomposites made of bimetallic nanoparticles and mesogenic metal alkanoates, Mater. Proc. 14 (1) (2023) 19, https://doi.org/10.3390/IOCN2023-14494.
[28] V. Rudenko, et al., Intensity-dependent optical nonlinearities of composite materials made of ionic liquid crystal glass and bimetallic nanoparticles, Liq. Cryst. 50 (1) (2023) 174–180, https://doi.org/10.1080/02678292.2022.2127952.
[29] D. Zhulai, et al., Exploring dielectric properties and polarization relaxation processes in ionic liquid crystals with synthesized carbon and gold nanoparticles, Mol. Cryst. Liq. Cryst. (2024) 1–12, https://doi.org/10.1080/15421406.2024.2348198.
[30] D. Zhulai, et al., Photoconductivity of ionic thermotropic liquid crystal with semiconductor nanoparticles, J. Mol. Liq. 267 (2018) 406–410, https://doi.org/10.1016/j.molliq.2017.12.097.
[31] Dmytro Zhulai, et al., Synthesis of carbon and gold nanoparticles in ionic liquid crystals: structural properties and electrical behavior for electro-optical sensors, Nano Sel. (2025) e202400063, https://doi.org/10.1002/nano.202400063.

[32] Ogenko Volodymyr, et al., Synthesis and spectral characteristics of Cu (II), Ni (II) and Fe (III) nanosized complexes on the surface of carbon quantum dot, Ukr. Chem. J. 87 (9) (2021) 3–13, https://doi.org/10.33609/2708-129X.87.09.2021.3-13.
[33] J. Tauc, Radu Grigorovici, Anina Vancu, Optical properties and electronic structure of amorphous germanium, Phys. Status Solidi (b) 15 (2) (1966) 627–637, https://doi.org/10.1002/pssb.19660150224.
[34] D. Viezbicke Brian, et al., Evaluation of the Tauc method for optical absorption edge determination: znO thin films as a model system, Phys. Status Solidi (b) 252 (8) (2015) 1700–1710, https://doi.org/10.1002/pssb.201552007.
[35] Chukwuocha Ephrem O., Michael C. Onyeaju, and Taylor ST Harry. "Theoretical studies on the effect of confinement on quantum dots using the brus equation." (2012). https://doi.org/10.4236/wjcmp.2012.22017.
[36] Neto ES Freitas, et al., Temperature-dependent Raman study of thermal parameters in CdS quantum dots, Nanotechnology 23 (12) (2012), https://doi.org/10.1088/0957-4484/23/12/125701.
[37] V.M. Asaula, et al., Mesomorphic and glass formed properties of homologous series of cadmium alkanoates, Ukr Chem. 485 (2011) 24–27.
[38] Santos Elton JG, Efthimios Kaxiras, Electric-field dependence of the effective dielectric constant in graphene, Nano Lett. 13 (3) (2013) 898–902, https://doi.org/10.1021/nl303611v.
[39] McCann Edward, Mikito Koshino, The electronic properties of bilayer graphene, Rep. Prog. Phys. 76 (5) (2013) 056503, https://doi.org/10.1088/0034-4885/76/5/056503.
[40] T. Margraf Johannes, et al., The electronic structure of amorphous carbon nanodots, J. Phys. Chem. B 119 (24) (2015) 7258–7265, https://doi.org/10.1021/jp510620j.
[41] Kundu Arpan, et al., Quantum vibronic effects on the electronic properties of solid and molecular carbon, Phys. Rev. Mater. 5 (7) (2021) L070801, https://doi.org/10.1103/PhysRevMaterials.5.L070801.
[42] D.S. Zhulai, et al., Structural characteristics of different types of nanoparticles synthesised in mesomorphic metal alkanoates, Liq. Cryst. 44 (8) (2017) 1269–1276, https://doi.org/10.1080/02678292.2016.1276979.
[43] G. Gurevich Yu, et al., Dember effect: problems and solutions, Phys. Lett. A 377 (38) (2013) 2673–2675, https://doi.org/10.1016/j.physleta.2013.08.003.
[44] Goldman S. Robert, et al., Dember-effect theory, J. Appl. Phys. 49 (5) (1978) 2849–2854, https://doi.org/10.1063/1.325166.
[45] Seeger Karlheinz. "Semiconductor physics: an introduction." (2004). https://doi.org/10.1007/978-3-662-03797-3.
[46] Choi Jongwan, et al., Bandgap engineering of nanosized carbon dots through electron-accepting functionalization, J. Ind. Eng. Chem. 65 (2018) 104–111, https://doi.org/10.1016/j.jiec.2018.04.018.
[47] Zhou Zhishan, et al., Energy transfer mediated enhancement of room-temperature phosphorescence of carbon dots embedded in matrixes, Adv. Opt. Mater. 10 (1) (2022) 2100704, https://doi.org/10.1002/adom.202100704.
[48] Li Ming, et al., Carbon quantum dots decorated Cu 2 S nanowire arrays for enhanced photoelectrochemical performance, Nanoscale 8 (16) (2016) 8559–8567, https://doi.org/10.1039/C5NR06908D.
[49] Yu Xiao-Yun, et al., High performance and reduced charge recombination of CdSe/CdS quantum dot-sensitized solar cells, J. Mater. Chem. 22 (24) (2012) 12058–12063, https://doi.org/10.1039/C2JM16738G.
[50] Badawi Ali, Decrease of back recombination rate in CdS quantum dots sensitized solar cells using reduced graphene oxide, Chin. Phys. B 24 (4) (2015) 047205, https://doi.org/10.1088/1674-1056/24/4/047205.